RSC Advances

PAPER

View Article Online
View Journal | View Issue

Cite this: *RSC Adv.*, 2024, **14**, 7528

Magnetic $MnFe_2O_4$/ZIF-67 nanocomposites with high activation of peroxymonosulfate for the degradation of tetracycline hydrochloride in wastewater

Si Lu, Sasha You, Junhao Hu, Xiang Li and Ling Li *

Advanced oxidation processes (AOPs) based on PMS have been used to degrade various refractory pollutants such as drugs, endocrine disruptors, dyes and perfluorinated compounds due to their wide application range, mild reaction conditions, fast reaction rate and simple operation. In this study, tetracycline hydrochloride (TCH) was degraded based on this method. Magnetic $MnFe_2O_4$/ZIF-67 nanocomposites were successfully prepared by a hydrothermal method, which combined the magnetic separation characteristics of $MnFe_2O_4$ with the high catalytic activity of ZIF-67 and were used to activate peroxymonosulfate (PMS) to efficiently degrade TCH. Satisfactory removal results were obtained with this simple and readily available material, with 82.6% of TCH removed in 15 min. The effect of different conditions on the degradation effect was investigated, and the optimal catalyst concentration and PMS concentration were determined to be 0.1 g L^{-1} and 0.2 g L^{-1}, respectively, and all had good degradation effects at pH 5 to 10. XPS, impedance test and radical quenching experiments were used to investigate the degradation mechanism. The results showed that sulfate radical ($SO_4^{-\bullet}$) was the main active species in the degradation process. In addition, the catalyst has good cyclic stability, which provides a new idea for the removal of TCH in wastewater. It is worth mentioning that the catalyst also has good degradation property for other pollutants.

Received 13th December 2023
Accepted 21st February 2024

DOI: 10.1039/d3ra08511b

rsc.li/rsc-advances

1 Introduction

In recent decades, with the continuous development of the social economy and the rapid improvement of production capacity, the ensuing environmental problems have become increasingly serious.[1,2] Water environmental pollution has attracted more and more attention.[3] Tetracycline hydrochloride (TCH) is a representative broad-spectrum antibiotic, widely used in clinical therapy, aquaculture, animal husbandry, and other fields.[4–7] Overuse of TCH causes it to accumulate in large quantities in wastewater, posing a serious threat to the ecosystems and human health.[8,9] Due to its stable chemical structure and antibacterial properties, it is difficult to biodegrade, so it is urgently required to find more effective ways to degrade TCH in wastewater.[10,11]

Researchers have found a variety of methods to remove TCH, including adsorption,[12] membrane separation,[13] biodegradation,[14] and advanced oxidation processes.[15,49] Compared with other methods, AOPs have the advantages of simple operation, fast and efficient response and environmental friendliness, and have attracted more and more attention.[16–19] Common oxidants of AOPs include peroxymonosulfate (PMS), peroxydisulfate (PDS), and hydrogen peroxide (H_2O_2). Because PMS is more easily activated than PDS,[20] and compared with $^{\bullet}OH$ produced by H_2O_2, $SO_4^{-\bullet}$ produced by PMS has the advantages of long life, good selectivity, and wide working pH range;[21–24] as such, the type of AOPs based on PMS activation to generate active radicals has received wide attention.[50,51] Many transition metal ions (such as Co^{2+}, Fe^{3+}, Cu^{2+}, and Mn^{2+}) can effectively activate PMS to produce active free radicals, among which cobalt ions have been reported to have the best ability to activate PMS.[25–29] However, although the Co^{2+}/PMS system can degrade organic pollutants, it has the problem that homogeneous catalysts cannot be recovered, and carcinogenic Co^{2+} will have an impact on human health,[30] so it is particularly important to find cobalt-containing heterogeneous catalysts.

Metal–organic frameworks (MOFs) exhibit excellent performance in wastewater treatment due to their unique structure such as high specific surface area and large porosity.[31–37] ZIF-67, a mature cobalt-based MOF, has high thermal and chemical stability, which shows certain advantages in wastewater treatment.[46–48] For example, the microporous ZIF-67 synthesized by Liang *et al.* showed ultra-high adsorption capacity for the antibiotic CIP and successfully removed CIP.[38] Another example

Ministry-of-Education Key Laboratory for the Synthesis and Application of Organic Function Molecules, Hubei University, 430062, People's Republic of China. E-mail: lingli@hubu.edu.cn

is the synthesis of ZIF-67 by Dong *et al.*, which successfully achieved rapid degradation of carbamazepine in wastewater with a catalytic efficiency of eight times that of MnO_2.[39] However, although ZIF-67, the cobalt-containing multiphase catalyst, has a high catalytic efficiency, its difficulty in separating from wastewater limits its application.

Magnetic separation technology has become one of the most promising separation technologies due to its advantages of low cost and high efficiency. The magnetic MOF matrix composite material can comprehensively utilize the high porosity and high catalytic efficiency of MOFs and the magnetic separation characteristics of magnetic materials[40] so that the materials can be separated and recovered by external magnetic force while removing antibiotics from water. For magnetic materials, spinel ferrites XFe_2O_4 (X = Mn, Fe, Co, Ni, and Cu) have attracted great attention due to their significant nanometer size, high specific surface area, and superparamagnetic behavior.[41] One of the most impressive is the ferromanganite ($MnFe_2O_4$), which can not only achieve catalytic effects through the synergistic effect of Fe and Mn but also magnetic separation and recovery through its inherent magnetism.[42] However, the inherent magnetism of $MnFe_2O_4$ makes it easy to agglomerate, thus reducing its specific surface area and affecting the catalytic activity.[43] In addition, it is easy to cause excessive leaching of Mn^{2+}/Fe^{3+} resulting in secondary pollution, so it is a good choice to use some carriers to fix $MnFe_2O_4$.

Based on the above discussion, we combined $MnFe_2O_4$ and ZIF-67 to retain the high catalytic activity of Co-based MOFs ZIF-67; moreover magnetic separation and recovery could be carried out. Using PMS as an oxidant, the degradation of TCH in water by $MnFe_2O_4$/ZIF-67-activated PMS was investigated. The advantage of $MnFe_2O_4$/ZIF-67 material is that the material is simple and easy to obtain, requires only a short time to achieve efficient degradation, and can be reused by magnetic recycling.

2 Experimental

2.1 Chemicals and materials

Iron chloride hexahydrate ($FeCl_3 \cdot 6H_2O$), manganese chloride hexahydrate ($MnCl_3 \cdot 6H_2O$), cobalt nitrate hexahydrate ($Co(NO_3)_2 \cdot 6H_2O$), 2-methylimidazole (2-MIM), and tetracycline hydrochloride (TCH) were purchased from Macklin, China. Peroxymonosulfate (PMS) was obtained from Aladdin, China, and methanol (MeOH) was purchased from Shanghai Sinopharm Chemical Reagent Co., Ltd. All the reagents were used without further purification.

2.2 Synthesis of magnetic $MnFe_2O_4$

$FeCl_3 \cdot 6H_2O$ and $MnCl_3 \cdot 6H_2O$ were dispersed in a beaker containing ethylene glycol at a molar ratio of 2 : 1 and ultrasonically dissolved to obtain a transparent mixed solution. Then, the pre-prepared NaOH solution was gradually added to the above-mixed solution, and the pH value of the solution was monitored with a pH meter until the black slurry with pH > 10 was obtained. After stirring for 30 min, the slurry was transferred to a Teflon-lined autoclave at 200 °C for 24 h to obtain $MnFe_2O_4$.

2.3 Synthesis of magnetic composite $MnFe_2O_4$/ZIF-67

Solution A was formed by mixing 0.1 g $MnFe_2O_4$ and PVP with 30 mL methanol under ultrasound for 30 min. At the same time, 1.16 g of $Co(NO_3)_2 \cdot 6H_2O$ and 1.31 g of 2-methylimidazole were dissolved in 15 mL of methanol each at room temperature under ultrasound to form solution B and solution C, respectively,. Then, solution C was slowly added to solution A for ultrasonic mixing for 5 min, and solution B was added dropwise to the above dispersion. After 20 min of ultrasound, the mixture was transferred to a Teflon-lined autoclave at 120 °C for 6 h. Finally, the precipitate was collected using magnets, washed with methanol several times, and dried at 70 °C for 12 h.

2.4 Characterization

The surface morphology was observed by a JSM6510LV tungsten lamp scanning electron microscope (SEM, JEOL, Japan). The X-ray diffraction pattern of the sample was obtained using a D8-advanced X-ray diffractometer (XRD, Bruker, Germany) equipped with a Cu Kα source (40 mA, 40 kV). Fourier transform infrared spectroscopy (FTIR) in the region of 400–4000 cm^{-1} was measured on a single-frequency infrared spectrometer using the potassium bromide tablet technique. The oxidation states of Co, Fe and Mn in $MnFe_2O_4$/ZIF-67 were studied by X-ray photoelectron spectroscopy (XPS, Thermo, USA). The ultraviolet-visible spectrophotometer (752N, INESA, Shanghai) was used to measure the corresponding absorbance of the pollutant at 357 nm.

2.5 Degradation experiment

All experiments were conducted in a 100 mL beaker placed on a magnetic stirrer at room temperature. To avoid the effect of natural light on degradation, the beaker was wrapped in tin foil for dark treatment. Moreover, to evaluate the performance of the catalyst for activating PMS to degrade TCH, a certain amount of $MnFe_2O_4$/ZIF-67 was dispersed in a beaker containing 50 mL TCH solution, and appropriate PMS was immediately added to initiate the oxidation reaction. Then, within the specified time, an appropriate amount of the reaction solution was collected and quenched with 0.5 mL methanol to stop further reaction. The absorbance of the quenched solution at 357 nm was measured using a UV-vis spectrophotometer, and the residual TCH concentration was calculated according to the standard curve. In addition, all the optimization experiments, other conditions and steps were kept unchanged, and only the PMS concentration, catalytic concentration and initial pH value (adjusted by NaOH and HCl) were changed.

3 Results and discussion

3.1 Characterization

FT-IR spectra of $MnFe_2O_4$, ZIF-67 and $MnFe_2O_4$/ZIF-67 are shown in Fig. 1a. FT-IR spectrum of the $MnFe_2O_4$/ZIF-67 composite was basically similar to that of ZIF-67, except that the absorption peak at 571 cm^{-1} was attributed to the Fe–O–Fe group in the $MnFe_2O_4$ particle, which indicated the successful doping of $MnFe_2O_4$. The absorption peak at 422 cm^{-1} was attributed to the Co–N

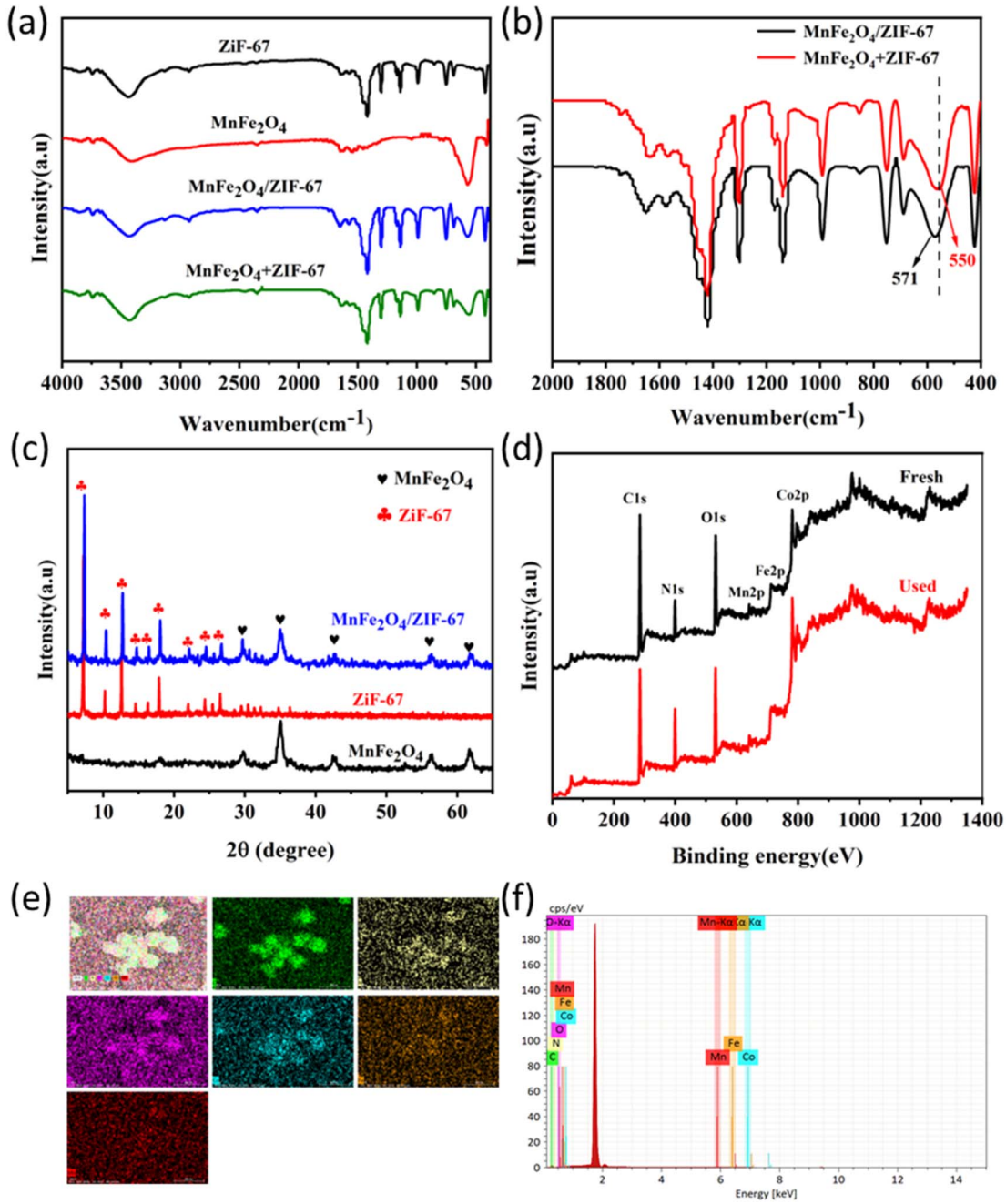

Fig. 1 (a) FT-IR spectra, and (c) XRD patterns of different as-prepared materials. (b) Locally magnified FT-IR spectra of the as-prepared $MnFe_2O_4$/ZIF-67 and $MnFe_2O_4$ + ZIF-67. (d) Full XPS spectra of the fresh and reacted as-prepared $MnFe_2O_4$/ZIF-67. (e) Elemental mapping of C, N, O, Co, Fe and Mn in $MnFe_2O_4$/ZIF-67. (f) EDS analysis of $MnFe_2O_4$/ZIF-67.

stretching vibrations of ZIF-67. The peaks at 1055 and 1390 cm^{-1} correspond to the presence of the benzene ring. The peaks at 1350–1500 cm^{-1} can be attributed to the stretching vibration of the imidazole ring, and the peaks at 900–1350 cm^{-1} can be attributed to the plane vibration of the imidazole ring. In addition, as shown in Fig. 1b, the peak position of $MnFe_2O_4$/ZIF-67 at 571 cm^{-1} is greatly shifted from that observed in the physical mixture of $MnFe_2O_4$ + ZIF-67. Therefore, it can be inferred that $MnFe_2O_4$/ZIF-67 is not a simple physical mixing. Instead, a new composite material was synthesized.

Fig. 1c shows the XRD patterns of $MnFe_2O_4$/ZIF-67, $MnFe_2O_4$ and ZIF-67 for a comparison. The diffraction peaks of $MnFe_2O_4$/ZIF-67 composites at 2θ = 30.2°, 35.7°, 43.3°, 57.2° and 62.8° were consistent with those of $MnFe_2O_4$ nanoparticles. Moreover, the diffraction peaks at 2θ = 7.4°, 10.4°, 12.8° and 18.0° correspond to the (011), (002), (112) and (222) Bragg planes of pure ZIF-67 crystals, respectively. This clearly confirms the successful preparation of the $MnFe_2O_4$/ZIF-67 composite, in which the inherent crystal structure of ZIF-67 is not significantly disturbed by the introduction of $MnFe_2O_4$ nanoparticles.

Fig. 1d shows the full XPS spectrum of $MnFe_2O_4$/ZIF-67 before and after the reaction, from which it can be seen that there are Co, Fe, Mn, C, N and O elements in $MnFe_2O_4$/ZIF-67, which further confirmed the successful synthesis of the composite material. Fig. 1e shows the element mapping of $MnFe_2O_4$/ZIF-67, in which C, N, O, Co, Fe and Mn also existed, which was also proven by EDS analysis of $MnFe_2O_4$/ZIF-67, as shown in Fig. 1f. They are consistent with the results of the full XPS spectrum, and also proved the successful synthesis of $MnFe_2O_4$/ZIF-67.

The structure and surface morphology of $MnFe_2O_4$/ZIF-67, $MnFe_2O_4$ and ZIF-67 were characterized by scanning electron microscopy and transmission electron microscopy. The SEM image of Fig. 2a shows that $MnFe_2O_4$ particles were small-sized nanoparticles, which were agglomerated because of their small particle size and strong magnetic interactions. It can be observed from Fig. 2b that the prepared ZIF-67 showed uniform rhombohedral dodecahedral crystal shapes with particle sizes between 500 and 600 nm, which was consistent with the literature reports.[44] Fig. 2c and d show that the surface of $MnFe_2O_4$/ZIF-67 was relatively rough compared to the morphology of ZIF-67, which may be due to the fact that $MnFe_2O_4$ was successfully compounded with ZIF-67. TEM images shown in Fig. 2e and f also clearly show the morphology of $MnFe_2O_4$/ZIF-67, and it was also found that $MnFe_2O_4$ and ZIF-67 were successfully compounded, and the size of ZIF-67 was consistent with the results of SEM images.

To explore the reasons for the rapid degradation efficiency of $MnFe_2O_4$/ZIF-67, impedance tests were conducted on $MnFe_2O_4$/ZIF-67, $MnFe_2O_4$ and ZIF-67 and the results are shown in Fig. 3a. It is clearly observed that $MnFe_2O_4$/ZIF-67 showed a smaller semicircle in the high frequency region than ZIF-67 and $MnFe_2O_4$, indicating an accelerated electron transfer rate.[45] Both Fe and Mn in the active metal center of $MnFe_2O_4$/ZIF-67 can promote the surface electron transfer rate and improve the degradation efficiency.

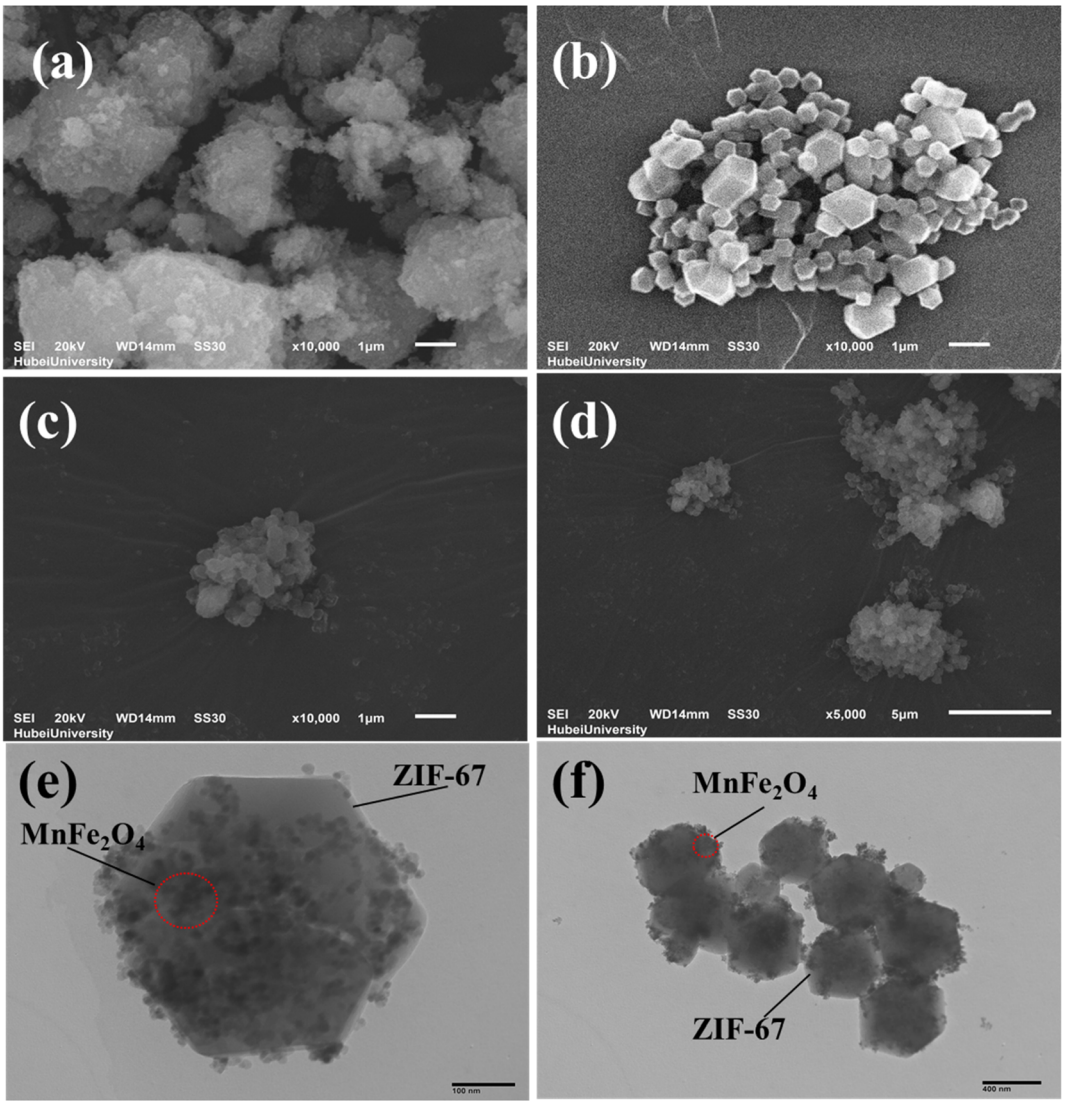

Fig. 2 SEM images of (a) $MnFe_2O_4$, (b) ZIF-67, and (c and d) $MnFe_2O_4$/ZIF-67. (e and f) TEM images of $MnFe_2O_4$/ZIF-67.

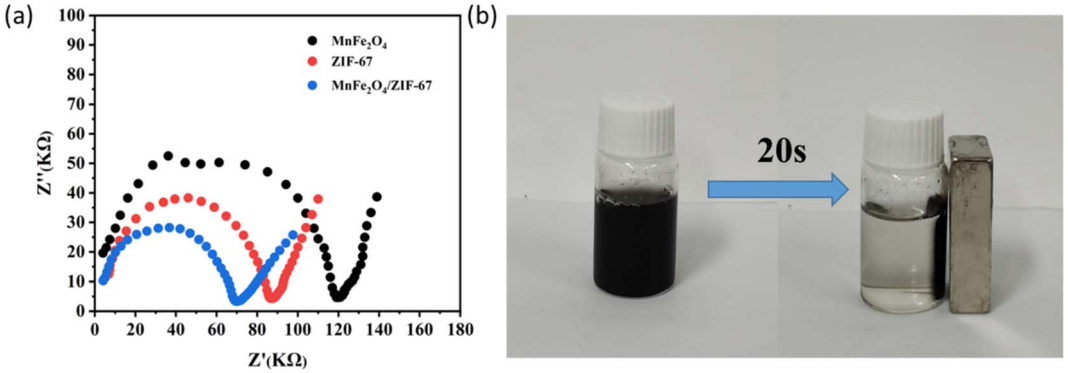

Fig. 3 (a) EIS plots of $MnFe_2O_4$, ZIF-67 and $MnFe_2O_4$/ZIF-67. (b) Magnetic recovery of $MnFe_2O_4$/ZIF-67.

The magnetic recovery ability of the catalyst was investigated by external magnetic force, as shown in Fig. 3b, and it was found that the $MnFe_2O_4$/ZIF-67 catalyst could be easily separated by a magnet within 20 s.

3.2 Catalytic performance

The removal effects of different catalysts on TCH were evaluated. The experimental conditions were 0.1 g per L catalyst, 0.2 g per L PMS and 20 mg per L TCH, and the pH value of the solution was 7.0. As shown in Fig. 4a, the TCH removal rate of pure ZIF-67 and $MnFe_2O_4$/ZIF-67 groups were 8.9% and 7.9%, within 30 min, respectively, indicating that the adsorption effect of materials on TCH was negligible. When no catalyst was added, only 20% of TCH was degraded in the presence of PMS alone. When both $MnFe_2O_4$ and PMS were added, the degradation efficiency of TCH was about 60% within 30 min. In addition, it can be observed that using the same dose of ZIF-67 and $MnFe_2O_4$/ZIF-67 to catalyze PMS, the degradation effect was almost similar at 87.2% and 88.3%, within 30 min, respectively. However, we were surprised to find that the degradation rate of TCH in the $MnFe_2O_4$/ZIF-67/PMS system was faster. In the first 6 min, the TCH removal rate using ZIF-67/PMS system was 34.3%, while the TCH removal rate using $MnFe_2O_4$/ZIF-67/PMS increased to 48.2%. It showed that $MnFe_2O_4$/ZIF-67/PMS could achieve rapid degradation in a short time. This phenomenon can be attributed to the fact that the introduction of $MnFe_2O_4$ can provide synergistic interaction between the two active metals and the cobalt in ZIF-67, thus promoting degradation. In addition, in the $MnFe_2O_4$/ZIF-67/PMS system, the removal rate of TCH can reach 82.6% in only 15 min, indicating the rapid degradation effect of the material.

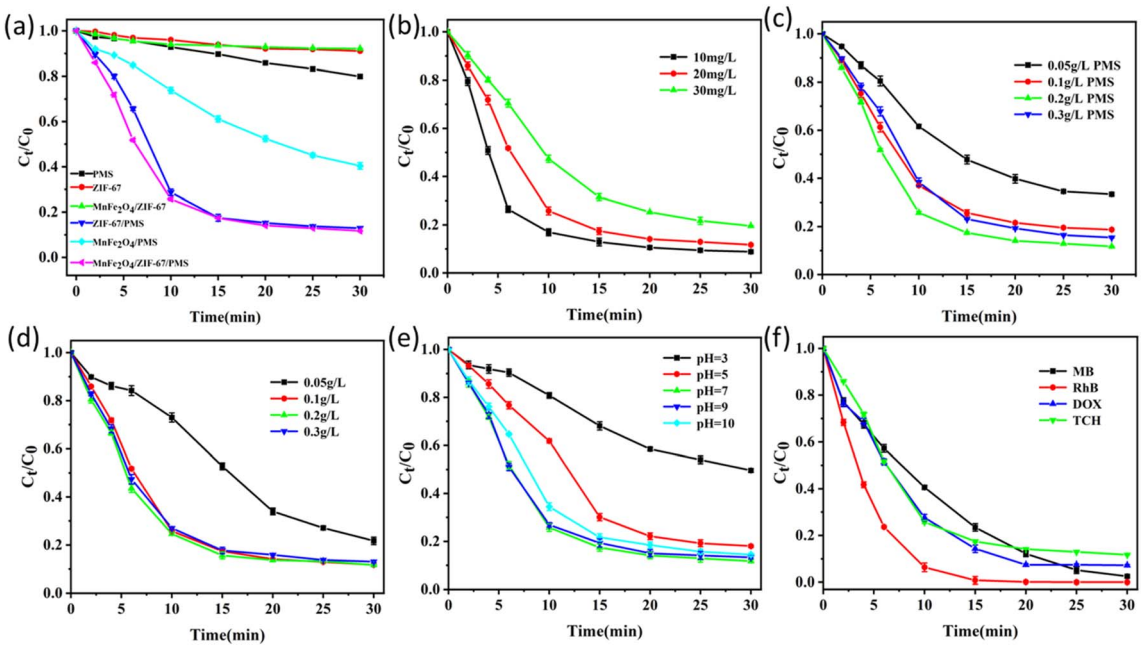

Fig. 4 (a) The degradation of TCH with different catalysts. The influence of (b) TCH, (c) PMS and (d) catalyst dosage, (e) initial pH for TCH removal and (f) the efficiencies of various contaminants in the $MnFe_2O_4$/ZIF-67/PMS system. [TCH] = 20 mg L^{-1} (for a and c–f), [PMS] = 0.2 g L^{-1} (for a, b, d and f), [catalyst] = 0.1 g L^{-1} (for a–c, e and f), T = 25 °C, initial pH = 7.0.

The effects of different conditions (initial TCH concentration, initial pH, PMS dose and catalytic dose) on TCH degradation were investigated. It can be seen from Fig. 4b that the degradation effect is greatly enhanced when the TCH concentration is reduced from 30 to 10 mg L^{-1}. This phenomenon can be attributed to the high concentration of pollutant molecules competing for the strong oxidizing free radicals produced by PMS activation. In addition, it has been reported that the intermediates generated by the side reaction consume part of the sulfate radical and hydroxyl radical, which also reduces the degradation rate of TCH.

Using PMS as the oxidant in this experiment, the effects of different amounts of PMS on TCH degradation were investigated, and the results are shown in Fig. 4c. When the concentration of PMS increased in the range of 0.05–0.2 g L^{-1}, the removal efficiency of TCH increased from 66.6% to 88.3% within 30 min. However, when the concentration of PMS continued to increase, the removal efficiency of TCH was significantly reduced. The improvement of TCH degradation efficiency and the rate are mainly due to the production of more active components. However, when the concentration of PMS continued to increase to 0.3 g L^{-1}, the removal efficiency of TCH decreased, which may be caused by the self-quenching of excess PMS. Therefore, 0.2 g per L PMS was selected for further experimental exploration.

The effects of different doses of $MnFe_2O_4$/ZIF-67 on TCH removal were investigated to determine the optimal dosage of the catalyst, as shown in Fig. 4d. The figure shows that when the amount of the catalyst is less than 0.1 g L^{-1}, only 50% of the TCH was degraded within 15 min, this is because active sites provided by a small amount of the catalyst were not rich, which affect the degradation effect. When the amount of the catalyst continued to exceed 0.1 g L^{-1}, the TCH degradation rate remained basically unchanged for 30 min. The possible reason for this phenomenon is that more catalysts will be clustered together and occupy part of the active sites. Therefore, 0.1 g per L $MnFe_2O_4$/ZIF-67 was selected for the catalytic degradation experiment.

The stability of PMS and the formation of free radicals were affected by different pH values of the solution. Therefore, the effects of different initial pH values (3–10) on TCH degradation efficiency in the $MnFe_2O_4$/ZIF-67/PMS system were studied. As can be seen from Fig. 4e, when the initial pH of the solution is neutral, the degradation of TCH in the $MnFe_2O_4$/ZIF-67/PMS system is as high as 88%. When it drops to 3, less than 50% of the TCH is removed. The unsatisfactory TCH degradation efficiency under super acidic conditions may be due to the fact that HSO_5^- is decomposed into sulfate instead of activating into a sulfate radical in the presence of excess hydrogen ions. Under the condition of peralkaline pH = 10, the degradation efficiency of TCH is about 85%, which is lower than the removal rate under neutral conditions. There may be two reasons for this phenomenon: first, PMS may self-decompose instead of generating sulfate radical, the specific process is shown in eqn (1) and (2). Second, under alkaline conditions, the active metal tends to produce hydroxide, resulting in the reduction of the active site.

$$HSO_5^- + SO_5^{2-} \rightarrow HSO_6^- + SO_4^{2-} \quad (1)$$

$$HSO_6^- + OH^- \rightarrow H_2O + SO_4^{2-} + O_2 \quad (2)$$

Finally, the suitability of the catalyst for other contaminants was also evaluated. DOX, RhB, MB and TCH were selected as pollutant models for the catalytic degradation experiments. It can be observed from Fig. 4f that the removal rate of the four pollutants reached more than 88% within 30 min, indicating that the degradation effect is good enough, and it also indicated the wide applicability of $MnFe_2O_4$/ZIF-67.

3.3 Degradation mechanism and pathway consideration

The ROS in the reaction solution was determined using a free radical quenching test to predict the reaction mechanism. Fig. 5a shows the effect of common scavengers such as methanol (MeOH), *tert*-butanol (TBA) and ethanol (EtOH) on TCH degradation in $MnFe_2O_4$/ZIF-67/PMS systems. Compared with the degradation amount without a quenching agent, the amount degraded after adding 100 mM of *tert*-butanol decreased slightly. After adding 100 mM of EtOH and MeOH, TCH dropped substantially with a degradation efficiency of only 65%. These results indicate that $SO_4^{-\bullet}$ and $^{\bullet}OH$ are the main active species in $MnFe_2O_4$/ZIF-67/PMS, but the former plays a dominant role.

To study the catalytic mechanism, the surface metal valence of the $MnFe_2O_4$/ZIF-67 catalyst was characterized by XPS spectroscopy. As shown in Fig. 5b, for pre-reaction Co, the peaks at 780.4 eV (Co $2p_{3/2}$) and 795.7 eV (Co $2p_{1/2}$) correspond to Co^{2+}, and the peaks at 782.0 eV (Co $2p_{3/2}$) and 797.3 eV (Co $2p_{1/2}$) correspond to Co^{3+}. The contents of Co^{2+} and Co^{3+} were 63.88% and 36.12%, respectively. For the Co after the reaction, the peak positions did not significantly shift. The peaks at 780.4 eV (Co $2p_{3/2}$) and 795.8 eV (Co $2p_{1/2}$) correspond to Co^{2+}, and the peaks at 781.7 eV (Co $2p_{3/2}$) and 797.3 eV (Co $2p_{1/2}$) correspond to Co^{3+}. The contents of Co^{2+} and Co^{3+} were 43.54% and 56.46%, respectively. The decrease of Co^{2+} content and the increase of Co^{3+} content after the reaction indicate that Co^{2+} was converted to Co^{3+} during the reaction. Fig. 5c shows the change of Fe valence content on the catalyst surface before and after the reaction. Before the reaction, the two main peaks of Fe $2p_{3/2}$ at 710.5 eV and 712.6 eV correspond to Fe^{2+} and Fe^{3+}, respectively. After the reaction, the peak area changed but there was no obvious peak shift. The two main peaks of Fe $2p_{3/2}$ at 710.3 eV and 712.8 eV correspond to Fe^{2+} and Fe^{3+}, respectively. The relative content of Fe^{2+} increased from 53.25% to 56.98%, and the relative content of Fe^{3+} decreased from 46.75% to 43.02%. As can be seen from Fig. 5d, the two main peaks of Mn $2p_{3/2}$ at 640.2 eV and 641.7 eV correspond to Mn^{2+} and Mn^{3+}, respectively, and no significant Mn^{4+} was detected, and the contents of Mn^{2+} and Mn^{3+} were 49.71% and 50.29%, respectively. The three main peaks of Mn $2p_{3/2}$ at 640.2, 641.3 and 642.6 eV correspond to Mn^{2+}, Mn^{3+} and Mn^{4+}, respectively, and the contents of Mn^{2+}, Mn^{3+} and Mn^{4+} were 34.09%, 36.21% and 29.70%, respectively. After the reaction, Mn^{4+} appeared and the contents of Mn^{3+} and Mn^{2+} decreased, indicating that Mn changed from a low valence state to a high valence state during

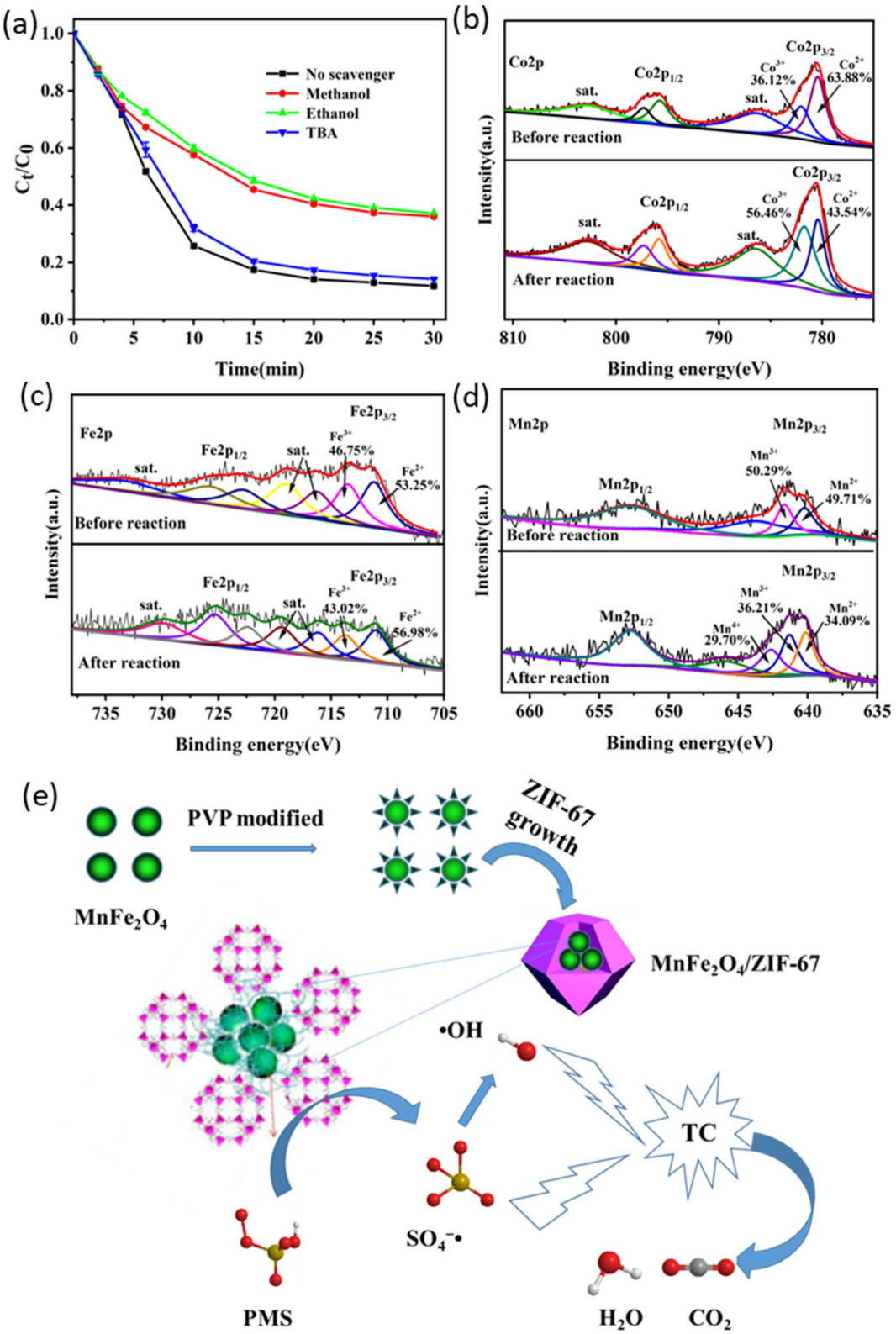

Fig. 5 (a) Quenching experiment on TCH degradation. XPS survey spectra of (b) Co 2p, (c) Fe 2p, and (d) Mn 2p of $MnFe_2O_4$/ZIF-67 before and after the reaction. (e) Schematic diagram of the degradation process.

the reaction. These results indicate that there were redox reactions of Co^{3+}/Co^{2+}, Fe^{3+}/Fe^{2+} and $Mn^{2+}/Mn^{3+}/Mn^{4+}$ in the $MnFe_2O_4$/ZIF-67/PMS system.

Based on the above results, the TCH degradation mechanism of the $MnFe_2O_4$/ZIF-67/PMS system can be briefly summarized as follows:

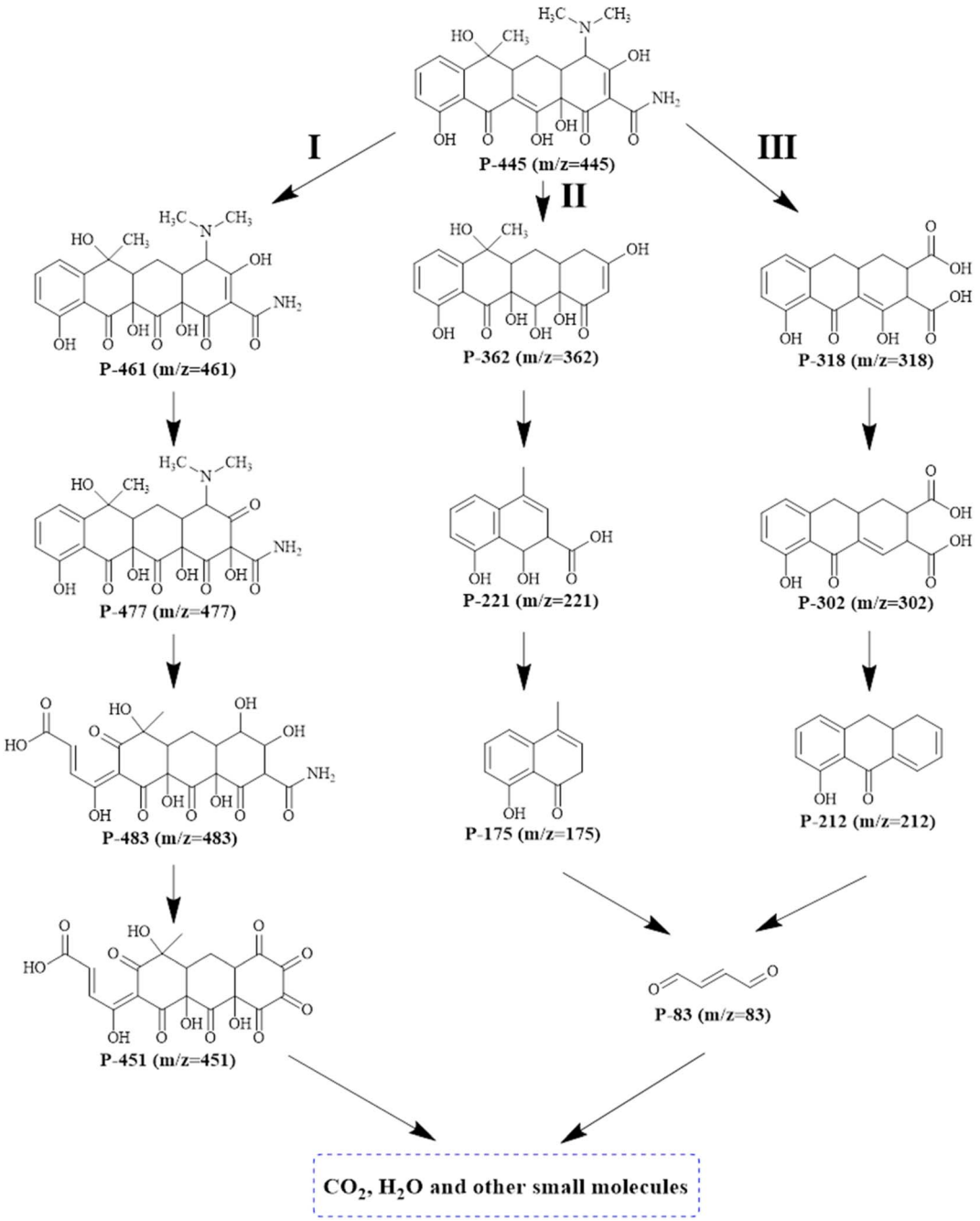

Fig. 6 Proposed pathways for TCH degradation in the $MnFe_2O_4$/ZIF-67/PMS system.

$$HSO_5^- + Co^{2+} \rightarrow SO_4^{-\bullet} + Co^{3+} + OH^- \quad (3)$$

$$HSO_5^- + Fe^{2+} \rightarrow SO_4^{-\bullet} + Fe^{3+} + OH^- \quad (4)$$

$$HSO_5^- + Mn^{2+} \rightarrow SO_4^{-\bullet} + Mn^{3+} + OH^- \quad (5)$$

$$HSO^{5-} + Mn^{3+} \rightarrow SO_4^{-\bullet} + Mn^{4+} + OH^- \quad (6)$$

$$Fe^{2+} + Mn^{3+} \rightarrow Fe^{3+} + Mn^{2+} \quad (7)$$

$$Fe^{3+} + Mn^{3+} \rightarrow Fe^{2+} + Mn^{4+} \quad (8)$$

$$HSO_5^- + Co^{3+} \rightarrow SO_5^{-\bullet} + H^+ + Co^{2+} \quad (9)$$

$$HSO_5^- + Fe^{3+} \rightarrow SO_5^{-\bullet} + H^+ + Fe^{2+} \quad (10)$$

$$HSO_5^- + Mn^{3+} \rightarrow SO_5^{-\bullet} + H^+ + Mn^{2+} \quad (11)$$

$$HSO_5^- + Mn^{4+} \rightarrow SO_5^{-\bullet} + H^+ + Mn^{3+} \quad (12)$$

$$SO_4^{-\bullet} + H_2O \rightarrow SO_4^{2-} + {}^{\bullet}OH + H^+ \quad (13)$$

$$2SO_5^{-\bullet} + 2OH^- \rightarrow 2SO_4^{2-} + 2{}^{\bullet}OH + 2O_2 \quad (14)$$

$SO_4^{-\bullet}/{}^{\bullet}OH + TCH \rightarrow$ intermediate product $\rightarrow H_2O + CO_2$(15)

First, HSO_5^- attacks the highly active metal reaction site provided by $MnFe_2O_4$/ZIF-67 to produce $SO_4^{-\bullet}$ (see eqn (3)–(8)), which is a similar process to the generation of hydroxyl radicals in the Fenton reaction. The excess HSO_5^- reacts with the high-valence metal center on the surface of $MnFe_2O_4$/ZIF-67 to form $SO_5^{-\bullet}$ (see eqn (9)–(12)), thus contributing to the cycle of Co^{3+}/Co^{2+}, Fe^{3+}/Fe^{2+}, and $Mn^{2+}/Mn^{3+}/Mn^{4+}$. In addition, $SO_4^{-\bullet}$ reacts with water, and $SO_5^{-\bullet}$ reacts with OH^- to produce another $^{\bullet}OH$ that can remove pollutants (see eqn (13) and (14)). Eventually, TCH molecules come into contact with $SO_4^{-\bullet}$ and $^{\bullet}OH$ and break them down into small inorganic molecules such as CO_2 and water (see eqn (15)). The degradation process is shown in Fig. 5e.

Possible degradation pathways of TCH were analyzed with LC-MS. As shown in Fig. 6, TCH first dissociated into P-445 (tetracycline). In the pathway I, the free radical attacked the double bond in the C-ring to form the product P-416, the C-ring double bond in P-416 was attacked by the free radical to form the intermediate P-477,[52] and the C-ring double bond of P-477 was attacked to open the ring to form the intermediate P-483, and then the amino group was eliminated to form P-451. In pathway II, the double bond in the C-ring of P-445 was attacked and the $-N(CH_3)_2$ and $-CONH_2$ groups were eliminated to form the intermediate P-362, after which the ring was opened to form P-211, and P-221 was further oxidized to form small molecules P-175 and P-83. In pathway III, P-445 formed the intermediate P-318 through dealkylation and ring-opening, and P-318 dehydroxized to form P-302, which was further oxidized to small molecules of P-212 and P-83. These intermediates and small molecules eventually decomposed into CO_2, H_2O and other small molecules.

3.4 Cyclic experiment of $MnFe_2O_4$/ZIF-67

The catalyst can be easily recovered with external magnetic force, and the stability of $MnFe_2O_4$/ZIF-67 was tested by four cycles of TCH removal experiments under the same conditions. As shown in Fig. 7a, the final removal efficiencies of TCH were 88.7%, 87.8%, 84.4% and 81.9%, respectively, indicating that $MnFe_2O_4$/ZIF-67 could still maintain good activity after repeated use.

The used $MnFe_2O_4$/ZIF-67 was also characterized by XRD and FT-IR. As shown in Fig. 7b and c, the used $MnFe_2O_4$/ZIF-67 and fresh $MnFe_2O_4$/ZIF-67 have almost the same XRD and FT-IR patterns, indicating that the structure of this catalyst does not

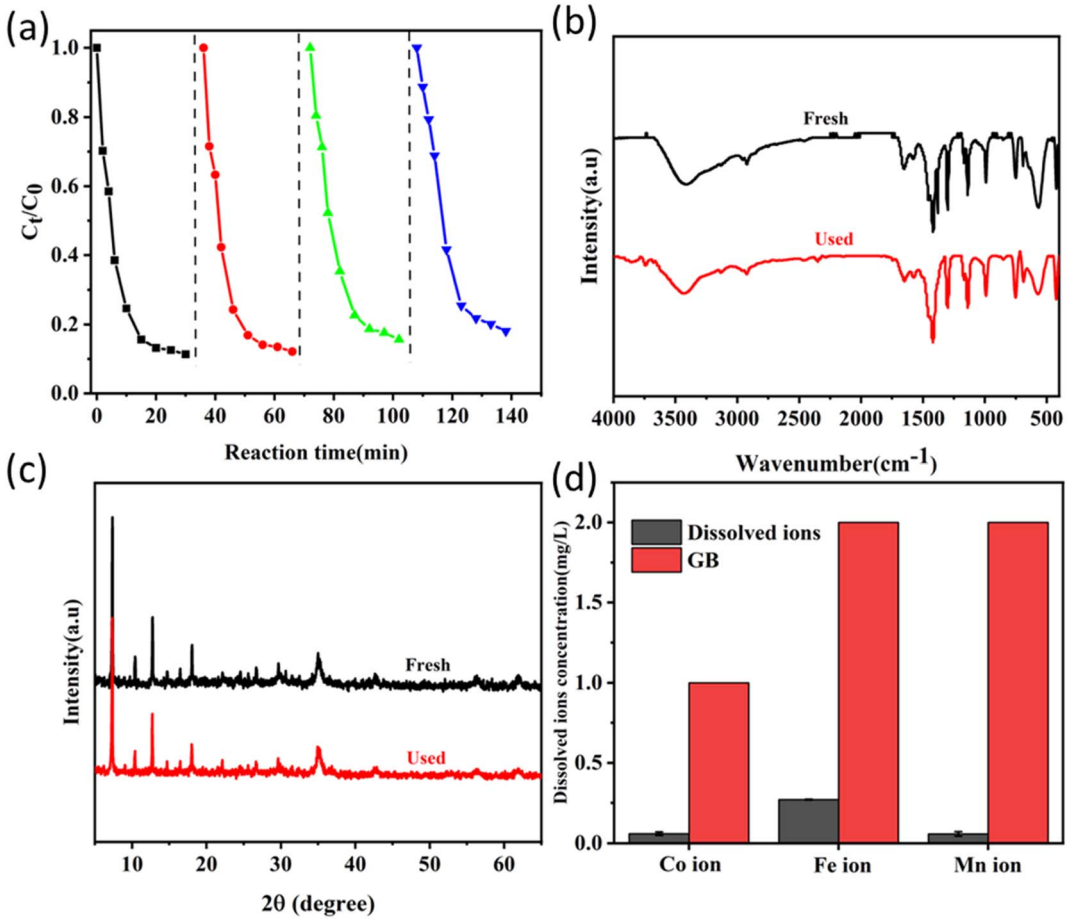

Fig. 7 (a) Degradation efficiency of TCH in four recycling of $MnFe_2O_4$/ZIF-67. (b) FT-IR and (c) XRD patterns of $MnFe_2O_4$/ZIF-67 before and after the reaction. (d) Ionic leaching rates of Co, Fe and Mn ions of $MnFe_2O_4$/ZIF-67 after the reaction and corresponding GB standards.

change significantly after the reaction, and it is a stable and durable catalyst.

The ion leaching rate after the degradation reaction is shown in Fig. 7d. The leaching ion concentrations of Co, Fe and Mn are 0.0600, 0.2704 and 0.0582 mg L^{-1} respectively, which are far lower than those in the corresponding Chinese wastewater discharge standard, which are 1 mg L^{-1} of Co (GB25476-2010), 2 mg L^{-1} of Fe (GB13456-2012) and 2 mg L^{-1} of Mn (GB8979-1996).

4 Conclusions

In summary, we synthesized magnetic composite $MnFe_2O_4$/ZIF-67 with high catalytic activity and used it as an activator of PMS to degrade TCH. Compared with pure $MnFe_2O_4$ and ZIF-67, $MnFe_2O_4$/ZIF-67 showed excellent catalytic performance. Under the optimal reaction conditions (initial pH value, the concentration of PMS and dosage of $MnFe_2O_4$/ZIF-67 were 7, 0.2 g L^{-1} and 0.1 g L^{-1}, respectively), TCH degradation efficiency reached 85.2%. In the cyclic experiment, the magnetic $MnFe_2O_4$/ZIF-67 catalyst could still maintain a good degradation effect after four cycles. The above results show that the catalyst has high catalytic activity, stability and magnetic recovery.

Author contributions

Si Lu: conceptualization, data curation, formal analysis, visualization, writing – original draft. Sasha You: investigation, software. Junhao Hu: methodology, data curation. Xiang Li: project administration. Ling Li: funding acquisition, supervision, validation, writing – review and editing.

Conflicts of interest

The authors declare that they have no known competing financial interests or personal relationships that could have appeared to influence the work reported in this paper.

Acknowledgements

This work was supported by Ministry-of-Education Key Laboratory for the Synthesis and Application of Organic Function Molecules, Hubei University.

References

1 I. Othman, J. H. Zain, M. A. Haija, *et al.*, Catalytic activation of peroxymonosulfate using CeVO4 for phenol degradation: an insight into the reaction pathway, *Appl. Catal., B*, 2020, **266**, 118601.

2 G. Wang, X. Nie, X. Ji, *et al.*, Enhanced heterogeneous activation of peroxymonosulfate by Co and N codoped porous carbon for degradation of organic pollutants: the synergism between Co and N, *Environ. Sci.: Nano*, 2019, **6**(2), 399–410.

3 Z. Frontistis, C. Drosou, K. Tyrovola, *et al.*, Experimental and modeling studies of the degradation of estrogen hormones in aqueous TiO2 suspensions under simulated solar radiation, *Ind. Eng. Chem. Res.*, 2012, **51**(51), 16552–16563.

4 B. Fan, Y. Tan, J. Wang, *et al.*, Application of magnetic composites in removal of tetracycline through adsorption and advanced oxidation processes (AOPs): a review, *Processes*, 2021, **9**(9), 1644.

5 J. Liu, S. Zhong, Y. Song, *et al.*, Degradation of tetracycline hydrochloride by electro-activated persulfate oxidation, *J. Electroanal. Chem.*, 2018, **809**, 74–79.

6 H. Zheng, Y. Hou, S. Li, *et al.*, Study on catalytic mechanisms of Fe3O4-rGOx in three typical advanced oxidation processes for tetracycline hydrochloride degradation, *Chin. Chem. Lett.*, 2023, **34**(1), 107253.

7 S. Li, W. Huang, P. Yang, *et al.*, One-pot synthesis of N-doped carbon intercalated molybdenum disulfide nanohybrid for enhanced adsorption of tetracycline from aqueous solutions, *Sci. Total Environ.*, 2021, **754**, 141925.

8 S. Li, Y. Yang, H. Zheng, *et al.*, Introduction of oxygen vacancy to manganese ferrite by Co substitution for enhanced peracetic acid activation and 1O2 dominated tetracycline hydrochloride degradation under microwave irradiation, *Water Res.*, 2022, **225**, 119176.

9 F. Sun, X. Yang, F. Shao, *et al.*, In-situ construction of Co (OH) 2 nanoparticles decorated biochar for highly efficient degradation of tetracycline hydrochloride via peracetic acid activation, *Chin. Chem. Lett.*, 2023, 108563.

10 G. Alnaggar, A. Hezam, Q. A. Drmosh, *et al.*, Sunlight-driven activation of peroxymonosulfate by microwave synthesized ternary MoO3/Bi2O3/g-C3N4 heterostructures for boosting tetracycline hydrochloride degradation, *Chemosphere*, 2021, **272**, 129807.

11 L. Zheng, Y. Gu, B. Hua, *et al.*, Hierarchical porous melamine sponge@ MIL-101-Fe-NH2 composite as Fenton-like catalyst for efficient and rapid tetracycline hydrochloride removal, *Chemosphere*, 2022, **307**, 135728.

12 G. Yang, Q. Gao, S. Yang, *et al.*, Strong adsorption of tetracycline hydrochloride on magnetic carbon-coated cobalt oxide nanoparticles, *Chemosphere*, 2020, **239**, 124831.

13 M. Liu, Y. Liu, D. Bao, *et al.*, Effective removal of tetracycline antibiotics from water using hybrid carbon membranes, *Sci. Rep.*, 2017, **7**(1), 43717.

14 Y. Ma, H. Xiong, Z. Zhao, *et al.*, Model-based evaluation of tetracycline hydrochloride removal and mineralization in an intimately coupled photocatalysis and biodegradation reactor, *Chem. Eng. J.*, 2018, **351**, 967–975.

15 Y. Chen, Y. Chen and X. Bai, 3D micro–meso-structured iron-based hybrid for peroxymonosulfate activation: performance, mechanism and comprehensive practical application potential evaluation, *Environ. Sci.: Water Res. Technol.*, 2022, **8**(11), 2602–2613.

16 Y. Zhao, Q. Li, H. Ren, *et al.*, Activation of persulfate by magnetic MnFe 2 O 4-bentonite for catalytic degradation of 2, 4-dichlorophenol in aqueous solutions, *Chem. Res. Chin. Univ.*, 2017, **33**, 415–421.

17 Y. Wang, L. Wang, Y. Zhang, *et al.*, Perdisulfate-assisted advanced oxidation of 2, 4-dichlorophenol by bio-inspired iron encapsulated biochar catalyst, *J. Colloid Interface Sci.*, 2021, **592**, 358–370.

18 J. O. Tijani, O. O. Fatoba, G. Madzivire, *et al.*, A review of combined advanced oxidation technologies for the removal of organic pollutants from water[J]. Water, Air, & *Soil Pollution*, 2014, **225**, 1–30.

19 L. Chen, H. Li and J. Qian, Degradation of roxarsone in UV-based advanced oxidation processes: A comparative study, *J. Hazard. Mater.*, 2021, **410**, 124558.

20 H. Sun, C. K. Kwan, A. Suvorova, *et al.*, Catalytic oxidation of organic pollutants on pristine and surface nitrogen-modified carbon nanotubes with sulfate radicals, *Appl. Catal., B*, 2014, **154**, 134–141.

21 X. Chen, W. Wang, H. Xiao, *et al.*, Accelerated TiO2 photocatalytic degradation of Acid Orange 7 under visible light mediated by peroxymonosulfate, *Chem. Eng. J.*, 2012, **193**, 290–295.

22 C. Cai, H. Zhang, X. Zhong, *et al.*, Ultrasound enhanced heterogeneous activation of peroxymonosulfate by a bimetallic Fe–Co/SBA-15 catalyst for the degradation of Orange II in water, *J. Hazard. Mater.*, 2015, **283**, 70–79.

23 W. Ren, J. Gao, C. Lei, *et al.*, Recyclable metal-organic framework/cellulose aerogels for activating peroxymonosulfate to degrade organic pollutants, *Chem. Eng. J.*, 2018, **349**, 766–774.

24 Z. Liu, Z. Gao and Q. Wu, Activation of persulfate by magnetic zirconium-doped manganese ferrite for efficient degradation of tetracycline, *Chem. Eng. J.*, 2021, **423**, 130283.

25 R. El Asmar, A. Baalbaki, Z. Abou Khalil, *et al.*, Iron-based metal organic framework MIL-88-A for the degradation of naproxen in water through persulfate activation, *Chem. Eng. J.*, 2021, **405**, 126701.

26 L. Dong, Y. Li, X. Chen, *et al.*, ZIF-67 loaded on Fe3O4-MnO2 as efficient peroxymonosulfate activator for rapid degradation of carbamazepine, *Adv. Mater. Interfaces*, 2021, **8**(11), 2100178.

27 H. Chi, X. He, J. Zhang, *et al.*, Hydroxylamine enhanced degradation of naproxen in Cu2+ activated peroxymonosulfate system at acidic condition: efficiency, mechanisms and pathway, *Chem. Eng. J.*, 2019, **361**, 764–772.

28 X. Zhang, X. Zhang, Y. Cai, *et al.*, Peroxymonosulfate-activated molecularly imprinted bimetallic MOFs for targeted removal of PAHs and recovery of biosurfactants from soil washing effluents, *Chem. Eng. J.*, 2022, **443**, 136412.

29 R. Luo, J. Wu, J. Zhao, *et al.*, ZIF-8 derived defect-rich nitrogen-doped carbon with enhanced catalytic activity for efficient non-radical activation of peroxydisulfate, *Environ. Res.*, 2022, **204**, 112060.

30 L. Hou, X. Li, Q. Yang, *et al.*, Heterogeneous activation of peroxymonosulfate using Mn-Fe layered double hydroxide: Performance and mechanism for organic pollutant degradation, *Sci. Total Environ.*, 2019, **663**, 453–464.

31 R. B. Lin, S. Xiang, W. Zhou, *et al.*, Microporous metal-organic framework materials for gas separation, *[J]. Chem*, 2020, **6**(2), 337–363.

32 Y. Wang, Z. Ao, H. Sun, *et al.*, Activation of peroxymonosulfate by carbonaceous oxygen groups: experimental and density functional theory calculations, *Appl. Catal., B*, 2016, **198**, 295–302.

33 X. Li, X. Huang, S. Xi, *et al.*, Single cobalt atoms anchored on porous N-doped graphene with dual reaction sites for efficient Fenton-like catalysis, *J. Am. Chem. Soc.*, 2018, **140**(39), 12469–12475.

34 E. GilPavas, S. Correa-Sanchez and D. A. Acosta, Using scrap zero valent iron to replace dissolved iron in the Fenton process for textile wastewater treatment: Optimization and assessment of toxicity and biodegradability, *Environ. Pollut.*, 2019, **252**, 1709–1718.

35 X. Jia, X. Chen, Y. Liu, *et al.*, Hydrophilic Fe3O4 nanoparticles prepared by ferrocene as high-efficiency heterogeneous Fenton catalyst for the degradation of methyl orange, *Appl. Organomet. Chem.*, 2019, **33**(4), e4826.

36 H. Kaur, S. Sinha, V. Krishnan, *et al.*, Photocatalytic reduction and recognition of Cr (VI): new Zn (II)-based metal–organic framework as catalytic surface, *Ind. Eng. Chem. Res.*, 2020, **59**(18), 8538–8550.

37 N. Liu, W. Dai, F. Fei, *et al.*, Insights into the photocatalytic activation persulfate by visible light over ReS2/MIL-88B (Fe) for highly efficient degradation of ibuprofen: Combination of experimental and theoretical study, *Sep. Purif. Technol.*, 2022, **297**, 121545.

38 C. Liang, X. Zhang, P. Feng, *et al.*, ZIF-67 derived hollow cobalt sulfide as superior adsorbent for effective adsorption removal of ciprofloxacin antibiotics, *Chem. Eng. J.*, 2018, **344**, 95–104.

39 L. Dong, Y. Li, X. Chen, *et al.*, ZIF-67 loaded on Fe3O4-MnO2 as efficient peroxymonosulfate activator for rapid degradation of carbamazepine, *Adv. Mater. Interfaces*, 2021, **8**(11), 2100178.

40 H. Alamgholiloo, S. Rostamnia, K. Zhang, *et al.*, Boosting aerobic oxidation of alcohols via synergistic effect between TEMPO and a composite Fe3O4/Cu-BDC/GO nanocatalyst, *ACS Omega*, 2020, **5**(10), 5182–5191.

41 H. Zhu, S. Zhang, Y. X. Huang, *et al.*, Monodisperse M x Fe3–x O4 (M= Fe, Cu, Co, Mn) nanoparticles and their electrocatalysis for oxygen reduction reaction, *Nano Lett.*, 2013, **13**(6), 2947–2951.

42 Y. Yao, Y. Cai, F. Lu, *et al.*, Magnetic recoverable MnFe2O4 and MnFe2O4-graphene hybrid as heterogeneous catalysts of peroxymonosulfate activation for efficient degradation of aqueous organic pollutants, *J. Hazard. Mater.*, 2014, **270**, 61–70.

43 J. Deng, S. F. Feng, X. Ma, *et al.*, Heterogeneous degradation of Orange II with peroxymonosulfate activated by ordered mesoporous MnFe2O4, *Sep. Purif. Technol.*, 2016, **167**, 181–189.

44 H. Alamgholiloo, B. Hashemzadeh, N. N. Pesyan, *et al.*, A facile strategy for designing core-shell nanocomposite of ZIF-67/Fe3O4: a novel insight into ciprofloxacin removal from wastewater, *Process Saf. Environ. Prot.*, 2021, **147**, 392–404.

45 J. Hu, Q. Yi, Z. Xiao, *et al.*, Synthesis of bimetal MOFs for rapid removal of doxorubicin in water by advanced oxidation method, *RSC Adv.*, 2022, **12**(55), 35666–35675.
46 M. Wang, Y. Sun, C. Huang, *et al.*, Nanoporous anodic aluminum oxide-confined ZIF-67 for efficiently activating peroxymonosulfate to degrade organic pollutants, *Sep. Purif. Technol.*, 2023, **318**, 123946.
47 L. Peng, X. Gong, X. Wang, *et al.*, In situ growth of ZIF-67 on a nickel foam as a three-dimensional heterogeneous catalyst for peroxymonosulfate activation, *RSC Adv.*, 2018, **8**(46), 26377–26382.
48 J. Xie, X. Luo, L. Chen, *et al.*, ZIF-8 derived boron, nitrogen co-doped porous carbon as metal-free peroxymonosulfate activator for tetracycline hydrochloride degradation: Performance, mechanism and biotoxicity, *Chem. Eng. J.*, 2022, **440**, 135760.
49 X. Xu, W. Shao, G. Tai, *et al.*, Single-atomic Co-N site modulated exciton dissociation and charge transfer on covalent organic frameworks for efficient antibiotics degradation via peroxymonosulfate activation, *Sep. Purif. Technol.*, 2024, **333**, 125890.
50 S. Wang and Y. Zhang, Zero valent iron-electro-Fenton-peroxymonosulfate (ZVI-E-Fenton-PMS) process for industrial wastewater treatment, *RSC Adv.*, 2023, **13**(22), 15063–15076.
51 Y. Zhang, G. Wu, F. Feng, *et al.*, Synergetic effects of in-plane and interlayer dual regulation on sandworm-like graphitic carbon nitride for high-efficiency photocatalytic performance, *Opt. Mater.*, 2024, **147**, 114742.
52 S. Han, P. Xiao, L. An, *et al.*, Oxidative degradation of tetracycline using peroxymonosulfate activated by cobalt-doped pomelo peel carbon composite, *Environ. Sci. Pollut. Res.*, 2022, **29**(15), 21656–21669.